J. Fluid Mech. (2003), *vol.* 484, *pp.* 41–68. © 2003 Cambridge University Press
DOI: 10.1017/S0022112003004002 Printed in the United Kingdom

On the validity of purely thermodynamic descriptions of two-phase cryogenic fluid storage

By CHARLES H. PANZARELLA[1]
AND MOHAMMAD KASSEMI[2]

[1]Ohio Aerospace Institute, Cleveland, OH 44142, USA

[2]National Center for Microgravity Research, NASA Glenn Research Center, Cleveland, OH 44135, USA

(Received 17 December 2001 and in revised form 31 July 2002)

This paper presents a comprehensive analysis of the transport processes that control the self-pressurization of a cryogenic storage tank in normal gravity. A lumped thermodynamic model of the vapour region is coupled with the Navier–Stokes and energy equations governing heat, mass and momentum transport in the liquid. These equations are discretized using a Galerkin finite-element method with implicit time integration. Three case studies are considered based on three different heating configurations imposed on the tank wall: liquid heating, vapour heating and uniform heating. For each case, the pressure and temperature rise in the vapour and the flow and temperature distributions in the liquid are determined. Results are compared to a lumped thermodynamic model of the entire tank. It is shown that the final rate of pressure rise is about the same in each case and close to that predicted by thermodynamics even though the actual pressures are different because of varying degrees of thermal stratification. Finally, a subcooled liquid jet is used to mix the liquid and limit the pressure rise. Even so, there is still some thermal stratification in the liquid, and as a result the final vapour pressure depends on the particular heat distribution.

1. Introduction

The extension of human space exploration from low Earth orbit into the solar system is one of NASA’s biggest challenges for the next millennium. The projected exploration programme includes a series of human and robotics expeditions to low- and high Earth orbit, the Moon, Mars and possibly to the asteroids and other planetary moons. Integral to all phases of these space and planetary expeditions is effective, affordable and reliable cryogenic fluid management for use in the propellant and life-support systems. Without safe and efficient cryogen storage, economically feasible and justified human missions will not be possible.

With the exception of extremely short-duration applications, significant cost savings can be achieved through reduction of launch mass by improving the cryogenic storage and transfer technologies (Salerno & Kittel 1999). Cryogen vaporization is one of the main causes of mass loss and self-pressurization in the storage tanks (Kittel & Plachta 2000). Vaporization can occur during the filling process or may be caused by heat leaks into the tank from the surrounding environment. Ordinarily, the excess pressure can be relieved by direct venting to the environment. For on-surface applications, such as those on the surfaces of the Earth, Moon or Mars, the relative position of liquid and vapour is well known. Therefore, continuous venting can be accomplished easily;

but over a significant length of time, it results in considerable cryogen mass loss. For in-Space applications, the spatial configuration of liquid and vapour is generally unknown, and direct venting without pre-positioning of the two phases is precluded because of the possibility of expelling liquid along with the vapour. Moreover, venting in Space is also undesirable because it prohibits manned flight operations around the storage tanks. Therefore, from both safety and cryogen conservation viewpoints, a ventless pressure control strategy is highly desirable for both on-surface and in-Space applications.

There are a number of experiments and thermodynamic studies of cryogen storage tanks in normal and reduced gravity. The most notable is due to Aydelott (1967), which shows that the rate of pressure rise is lower in reduced-gravity conditions because of an increase in the liquid-wetted wall areas and increased boiling. The experimental results were shown to lie somewhere between those obtained from two simplified thermodynamic analyses. In one thermodynamic model, the entire system of liquid and vapour is assumed to be at one temperature and pressure, and in the other all the heat entering the system is assumed to go directly into evaporation with the liquid temperature held constant. Further experimental work (Aydelott 1979, 1983) investigates the different liquid flow patterns resulting from an axial mixing jet. Dimensionless parameters are developed that characterize the four different liquid flow patterns observed and their effect on the bulk mixing behaviour.

Application of jet mixing to control the tank pressure is further investigated experimentally by Lin, Hasan & Van Dresar (1994). They show that the effects of natural-convection boundary layers forming at the wall on the vapour pressure rise can be countered by a subcooled jet flow emerging from the centre of the tank. They also conclude that a thermal equilibrium state is hard to achieve and that the existing correlations for mixing time and vapour-condensation rates based on small-scale tanks may not be applicable to large-scale liquid-hydrogen systems. The correct extrapolation can only be determined when the interaction between the forced and natural-convective flows is properly understood. The experimental investigations of Poth & Van Hook (1972) also show that there are significant departures from thermodynamic equilibrium and that a mixing jet could be used to minimize thermal stratification and reduce the tank pressure.

The effects of hybrid thermal control on the pressurization of a cryogenic propellant tank are investigated by Plachta (2000). It is shown experimentally that through effective use of passive insulation and active cryocooler technology, it is possible to control tank pressurization by establishing zero boil-off conditions at Earth's normal-gravity environment.

The theoretical and numerical treatments of cryogenic storage tanks can be divided into three main categories. The first category consists of tank pressurization studies that compute the pressure rise in the vapour mainly in terms of thermodynamic considerations. Lin & Hasan (1992) study self-pressurization of a partially filled liquid-hydrogen storage tank under microgravity conditions. The effects of tank size, liquid fill level and wall heat flux on the tank pressure rise are studied theoretically. They show that liquid thermal expansion tends to cause vapour condensation and wall heat flux leads to liquid evaporation at the interface. However, this approach is limited because the problem is assumed to be one-dimensional and there is no convection in the liquid. Vaughan & Schmidt (1991) performed a lumped analysis of a no-vent fill process in a ground-based environment. The model accounts for several major effects such as fluid inlet temperature, interfacial mass transfer and inlet jet characteristics that influence the fill process. It includes a semi-empirical condensation model based on universal submerged-jet theory that considers the condensation to be a function of bulk fluid properties and the liquid turbulence induced by the jet geometry and orientation. They show very good agreement between their model and some experimental results using Freon-114. Finally, Cha, Neiman & Hull (1993) perform a thermodynamic analysis of cryogen boil-off in a dewar and correlate the pressure variations in the container to latent heat of vaporization during an experiment with liquid helium.

The second category is composed of investigations that examine just the fluid flow and thermal stratification in the liquid cryogen without any thermodynamic consideration of the vapour phase. These investigations focus on the fluid flow in the liquid in terms of either mainly natural convection (Navickas 1988; Lin & Hasan 1990*a*; Grayson, Watts & Jurns 1997) or in terms of forced flows caused by jets or external thrusts (Hochstein, Gerhart & Aydelott 1984; Lin & Hasan 1990*b*; Grayson & Navickas 1993). In these representations, the transport processes in the vapour phase are also ignored, and the temperature of the liquid–vapour interface is assumed uniform and equal to its initial saturation value. Consequently, these investigations divulge no information with respect to the pressure rise in the vapour as a function of the various flow parameters in the liquid.

Finally, the third category of investigations examine mainly the behaviour and evolution of the liquid–vapour interface excluding any thermal or pressurization effects. The analyses are performed for both ground-based and microgravity applications and are mainly based on the Volume-of-Fluid (VOF) approach as embodied by the Los Alamos code RIPPLE and its derivatives (Kothe, Mjolsness & Torrey 1991). Investigations in this category have focused on: the evolution of the free surface as influenced by the microgravity environment (Liu 1994), the reorienting of the vapour subject to spacecraft thrust (Hung & Shyu 1992), the free surface deformation as affected by the jet flow and geysers (Kothe *et al.* 1991; Thornton & Hochstein 2001) or by external forces such as magnetic fields (Marchetta & Hochstein 2000; Marchetta, Hochstein & Sauter 2001) and fluid slosh coupled to gravity-gradient accelerations or spacecraft dynamics (Peterson, Crawley & Hansman 1989; Hung & Lee 1994). The studies in this category are all limited to isothermal models, and, again, divulge no information with regard to tank pressurization.

The present paper combines many of the features of these previous investigations in order to develop a more comprehensive model capable of determining how the flow parameters in the liquid affect the pressure rise in the vapour. This appears to be the first time that such a complete approach has been used. This is done by solving the full set of mass, momentum and energy equations in the liquid region coupled with a lumped thermodynamic model of the vapour region. The interface between the liquid and vapour regions is treated as a deformable free surface. The temperature and pressure in the vapour are considered to be spatially uniform but are permitted to change with time owing to any net heat and mass transfer across the boundaries.

The description of an idealized cryogenic tank and the development of its mathematical model are presented in § 2 along with a thermodynamic model of the entire tank and an identification of the most important dimensionless parameters. The liquid equations are solved by using the finite-element method with appropriately modified boundary conditions to account for the effects of the vapour region. This is briefly described in § 3. Finally, results are presented in § 4 for three different tank-wall heat distributions both with and without a jet. The vapour pressure rise is determined along with the temperature and flow fields in the liquid. These are compared to the results of a purely thermodynamic analysis.

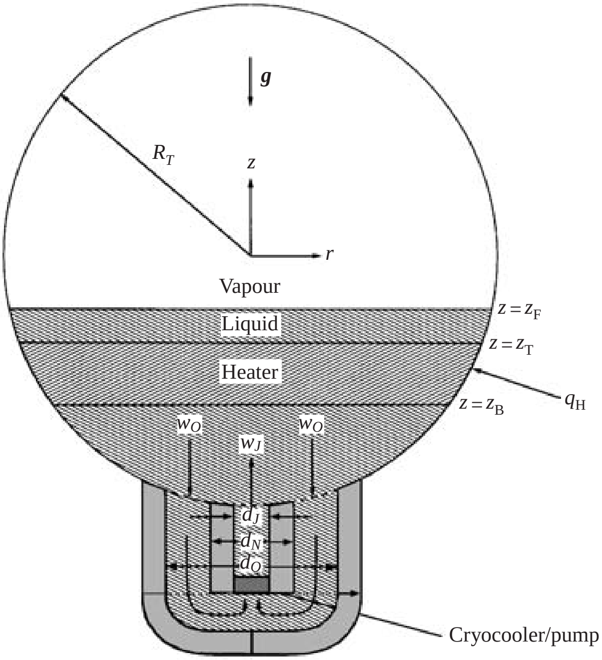

FIGURE 1. The geometry of an idealized spherical cryogenic tank. For the liquid-heating cases, a strip heater is placed up against the tank wall between $z = z_B$ and $z = z_T$. For the jet cases, liquid is forced upwards through an inlet at the bottom of the tank and removed from the surrounding outlet at the same flow rate. The temperature of the incoming jet fluid is controlled by using an external cryocooler.

2. Formulation of the mathematical model

The present model considers only ground-based applications where the strength of gravity is sufficient to keep the liquid beneath the vapour. This would apply to situations where the tank is placed on the surface of the Earth, Moon, Mars or other planetary body. The problem of in-Space applications is more difficult since the liquid has no preferred position in the tank, and there could be multiple isolated vapour bubbles moving around. The model developed herein would equally apply to these situations except that a more sophisticated method of keeping track of the free-surface position would be required. For the most part, the lumped treatment of the vapour region and its coupling with the liquid region would still hold.

The equilibrium arrangement of liquid and vapour for a ground-based spherical cryogenic tank of radius R_T is shown in figure 1. The origin of the coordinate system corresponds to the geometric centre of the tank and the negative z-axis is parallel to the gravity vector. The tank is filled with liquid up to a height z_F, the fill level, and saturated vapour occupies the remaining space above. The present work only considers those cases for which $z_F = 0$, which corresponds to a half-filled tank. Only solutions which are symmetric about the z-axis are permitted in order to reduce the computational burden. This motivates the use of cylindrical coordinates to describe the geometry. The domain of the numerical model is also restricted to the interior of the tank, neglecting all the external tubes and connections. Approximate boundary conditions are used where these external connections intersect with the tank wall.

2.1. *Liquid region*

The liquid is treated as an incompressible fluid with density ρ_L, dynamic viscosity μ_L, specific heat c_L and thermal conductivity k_L. These properties are evaluated at the normal boiling point temperature T_B. The effects of natural convection are accounted for by using the standard Boussinesq approximation, retaining the leading-order density variations only in the body force term in the Navier–Stokes equations. The coefficient of thermal expansion is denoted by β_L and the acceleration due to gravity by g. This is described by the following mass, momentum and energy equations for the liquid region,

$$\nabla \cdot \boldsymbol{u}_\mathrm{L} = 0, \tag{2.1}$$

$$\rho_\mathrm{L}\left(\frac{\partial \boldsymbol{u}_\mathrm{L}}{\partial t} + \boldsymbol{u}_\mathrm{L} \cdot \nabla \boldsymbol{u}_\mathrm{L}\right) = -\nabla p_\mathrm{L} + \mu_\mathrm{L}\nabla^2 \boldsymbol{u}_\mathrm{L} - \rho_\mathrm{L} g\left[1 - \beta_\mathrm{L}\left(T_\mathrm{L} - T_\mathrm{B}\right)\right]\boldsymbol{e}_z, \tag{2.2}$$

$$\rho_\mathrm{L} c_\mathrm{L}\left(\frac{\partial T_\mathrm{L}}{\partial t} + \boldsymbol{u}_\mathrm{L} \cdot \nabla T_\mathrm{L}\right) = k_\mathrm{L}\nabla^2 T_\mathrm{L}, \tag{2.3}$$

where $\boldsymbol{u}_\mathrm{L}$ is the liquid velocity, p_L is the liquid pressure, T_L is the liquid temperature and $\boldsymbol{e}_z$ is a unit vector pointing in the positive z direction.

2.2. *Boundary conditions at the liquid–vapour interface*

Conservation of mass requires the interfacial mass flux J due to evaporation or condensation to be equal to the rate at which liquid is flowing towards the interface,

$$J = \rho_\mathrm{L}\left(\boldsymbol{u}_\mathrm{L} - \boldsymbol{u}_\mathrm{I}\right) \cdot \boldsymbol{n}, \tag{2.4}$$

where $\boldsymbol{n}$ is the unit normal vector pointing into the vapour and $\boldsymbol{u}_\mathrm{I}$ is the interfacial velocity. There is a similar balance on the vapour side of the interface. According to this definition, J is positive for evaporation and negative for condensation. If $J = 0$, then this reduces to the more familiar form of the kinematic condition, which states that the fluid must be moving with the same velocity as the interface.

The no-slip condition requires the tangential component of liquid velocity to be equal to the tangential component of the interfacial velocity,

$$\left(\boldsymbol{u}_\mathrm{L} - \boldsymbol{u}_\mathrm{I}\right) \cdot \boldsymbol{t} = 0, \tag{2.5}$$

where $\boldsymbol{t}$ is a unit tangent vector at the interface.

A simplified energy boundary condition is obtained by balancing the energy required for phase change with the discontinuity in the heat flux,

$$LJ = \left(\boldsymbol{q}_\mathrm{L} - \boldsymbol{q}_\mathrm{V}\right) \cdot \boldsymbol{n}, \tag{2.6}$$

where L is the latent heat of vaporization (the enthalpy jump at constant temperature and pressure) and $\boldsymbol{q}_\mathrm{L} = -k_\mathrm{L}\nabla T_\mathrm{L}$ and $\boldsymbol{q}_\mathrm{V} = -k_\mathrm{V}\nabla T_\mathrm{V}$ are the heat-flux vectors on the liquid and vapour side of the interface, respectively. The most general form of this boundary condition also includes a term proportional to J^3 to account for the jump in kinetic energy, but this can be neglected compared to terms linear in J because the rate of evaporation is so small for the present cases. Other terms proportional to the viscosity are also negligible and are not included here. For a derivation of the most general form of this boundary condition, see Delhaye (1974).

A normal-stress balance across the interface, neglecting viscous stresses in the vapour and the momentum jump due to evaporation, simplifies to

$$p_\mathrm{L} - p_\mathrm{V} - 2\mu_\mathrm{L}\boldsymbol{S}_\mathrm{L} \cdot \boldsymbol{n} \cdot \boldsymbol{n} = 2H\sigma, \tag{2.7}$$

where p_V is the vapour pressure, σ is the interfacial surface tension, H is the mean curvature of the interface and $\boldsymbol{S}_L$ is the rate-of-strain tensor in the liquid defined by

$$\boldsymbol{S}_L = \tfrac{1}{2}\left[\nabla\boldsymbol{u}_L + (\nabla\boldsymbol{u}_L)^T\right], \tag{2.8}$$

where $\nabla\boldsymbol{u}_L$ and $(\nabla\boldsymbol{u}_L)^T$ are the velocity-gradient tensor and its transpose. This reduces to the familiar Young–Laplace equation when there is no fluid motion. The surface tension is assumed to be constant for this analysis, so the shear-stress boundary condition is just

$$\boldsymbol{S}_L \cdot \boldsymbol{n} \cdot \boldsymbol{t} = 0. \tag{2.9}$$

The viscous stress on the vapour side of the interface is neglected because the dynamic viscosity of the vapour is normally so much smaller than that of the liquid, $\mu_V \ll \mu_L$. This is similar to the one-sided model used by Burelbach, Bankoff & Davis (1988) to study the evaporation of thin liquid films.

If the liquid at the interface were in thermodynamic equilibrium with the adjacent vapour, then the interfacial temperature T_I would be equal to the saturation temperature T_S, which depends on the vapour pressure p_V according to this form of the Clausius–Clapeyron equation for an ideal gas,

$$T_S = \left(\frac{1}{T_B} - \frac{R_G}{Lm}\ln\frac{p_V}{p_B}\right)^{-1}, \tag{2.10}$$

where T_B is the normal boiling-point temperature at atmospheric pressure p_B, m is the molar mass of the vapour and R_G is the ideal-gas constant. The interface is not in equilibrium when there is evaporation or condensation, and the interfacial temperature must be different from its equilibrium value, even if this difference is small. This departure from equilibrium can be described by the following constitutive equation derived from kinetic theory (Schrage 1953),

$$\kappa J = T_I - T_S, \tag{2.11}$$

$$\kappa = \frac{1}{a p_V L}\left(\frac{8T_S^5 R_G^3}{m^3\pi}\right)^{1/2}, \tag{2.12}$$

where a is the accommodation coefficient, the fraction of incoming vapour molecules that are absorbed by the liquid. The value $a = 1$ is assumed here. For typical properties and evaporation rates, the left-hand side of (2.11) is normally negligible, leading to the simpler and more often used condition $T_I = T_S$, but there are circumstances, such as when the free surface meets a solid wall, where singularities might arise if the complete condition is not used (see Burelbach *et al.* 1988).

2.3. *Other boundary conditions*

Three different heat-flux distributions are prescribed on the tank wall similar to those used in the experiments of Aydelott (1967). For the liquid-heating case, a constant heat flux q_H is prescribed on the interior heater surface between $z_B < z < z_T$, which is completely submerged in the liquid and flush against the tank wall. This is approximated by simply prescribing the liquid heat flux directly on the tank wall,

$$\boldsymbol{q}_L \cdot \boldsymbol{n}_T = -q_H, \tag{2.13}$$

where $\boldsymbol{n}_T$ is the outward-pointing normal at the tank wall. The rest of the tank wall is perfectly insulated. For the vapour-heating case, this same amount of heat is released only within the vapour region. It doesn't matter exactly how this heat is distributed because the vapour is treated in a lumped fashion. For the uniform-heating case, a constant heat flux is applied uniformly over the entire tank wall. For all three cases, the total heat input is the same.

When the jet is used, it is forced into the liquid region through an opening at the bottom of the tank with inner diameter $d_{\rm J}$. The following parabolic velocity profile is prescribed at the jet entrance,

$$\boldsymbol{u}_{\rm L}\cdot\boldsymbol{e}_z = 2w_{\rm J}\left(1-\frac{4r^2}{d_{\rm J}^2}\right), \tag{2.14}$$

$$\boldsymbol{u}_{\rm L}\cdot\boldsymbol{e}_r = 0, \tag{2.15}$$

where $w_{\rm J}$ is the average jet speed. The jet entrance over which this boundary condition is applied is specifically defined as that portion of the spherical tank surface restricted by $r < d_{\rm J}/2$ and $z < 0$.

The total amount of liquid inside the tank is kept constant by removing it at the same flow rate $w_{\rm J}\pi(d_{\rm J}/2)^2$ through the outlet boundary, which is similarly defined as that portion of the spherical tank surface restricted by $r_{\rm N} < r < r_{\rm O}$ and $z < 0$. This is done by prescribing the following velocity profile on this boundary,

$$\boldsymbol{u}_{\rm L}\cdot\boldsymbol{e}_z = \tfrac{1}{2}w_{\rm J}d_{\rm J}^2\frac{\left(r^2-r_{\rm N}^2\right)/\left(r_{\rm O}^2-r_{\rm N}^2\right)-\log\left(r/r_{\rm N}\right)/\log\left(r_{\rm O}/r_{\rm N}\right)}{r_{\rm O}^2+r_{\rm N}^2-\left(r_{\rm O}^2-r_{\rm N}^2\right)/\log\left(r_{\rm O}/r_{\rm N}\right)}, \tag{2.16}$$

$$\boldsymbol{u}_{\rm L}\cdot\boldsymbol{e}_r = 0. \tag{2.17}$$

This is the exact solution for the flow between two cylinders with inner and outer radii $r_{\rm N} = d_{\rm N}/2$ and $r_{\rm O} = d_{\rm O}/2$, respectively. The temperature of the liquid at the jet inlet is set equal to the constant temperature $T_{\rm J}$. The outlet boundary is insulated for the liquid-heating and vapour-heating cases, but has a specified heat flux prescribed upon it for the uniform-heating case. The area of the jet inlet is excluded from the total tank area used to compute the heat flux in the uniform-heating case when the jet is used.

The boundary condition at the liquid–vapour-wall contact line is simply that its position be fixed to $z = z_{\rm F}$. This avoids dealing with all of the complexities required to model dynamic contact line motion, such as permitting slip in the vicinity of the contact point. For the cases considered here, the free-surface deflection is so small that the contact point would only move from its initial position by a negligible amount anyway. In order to have a consistent solution, it is not possible to fix both the position and contact angle simultaneously. Thus, the contact angle is not specified and is solved for as part of the problem. This contact angle may conflict with the actual contact angle, which is very close to zero for hydrogen, but it is unavoidable unless dynamic contact line motion is considered. It is expected and assumed that the exact shape of the interface near the contact point will not significantly affect the results presented here. Future work will include a consistent treatment of dynamic contact-line motion.

2.4. *Lumped vapour region*

The vapour is treated as an inviscid compressible ideal gas with spatially uniform temperature $T_{\rm V}$, pressure $p_{\rm V}$ and density $\rho_{\rm V}$. This is valid as long as the heat flow into the vapour region is sufficiently small. Even if there is some fluid flow and variable temperature distribution in the vapour, it is only the total vapour pressure that is important for determining the saturation temperature $T_{\rm S}$, and it will be shown that pressure variations due to any non-uniformity in the vapour region would be extremely small compared to the total thermodynamic pressure.

The total vapour pressure can be thought of as a uniform thermodynamic pressure plus perturbations due to dynamic and hydrostatic pressure changes. The thermodynamic pressure is normally many orders of magnitude greater than the dynamic and hydrostatic pressures. For instance, the dynamic pressure scale $\rho_V u_V^2/2$ based on a maximum jet speed of $u_V = 1\,\text{cm}\,\text{s}^{-1}$ is equal to 6.65×10^{-5} Pa, and the viscous pressure scale $\mu_V u_V/R_T$ is equal to 6.414×10^{-7} Pa. A typical hydrostatic pressure difference is equal to $\rho_V g R_T = 0.652$ Pa. These are negligible when compared to the typical thermodynamic pressure $p_B = 1.014 \times 10^5$ Pa, and they can be omitted when computing the corresponding saturation temperature using (2.10). Since the interfacial temperature is set equal to the saturation temperature, the interfacial temperature will be nearly constant even if there is some flow in the vapour or changes in the free-surface position. The only other way in which flow in the vapour may become important is by exerting a shear stress on the liquid or by deforming the free surface, but these effects would be small in the present situation.

The vapour density is related to the temperature and pressure through the ideal-gas law,

$$\rho_V = \frac{p_V m}{R_G T_V}. \tag{2.18}$$

Since the total pressure is nearly constant as explained in the previous paragraph, the relative change in density from its saturation value will be due mainly to any temperature variations in the vapour, $|\rho_V - \rho_S|/\rho_S \approx |T_V - T_S|/T_S$. In order for the variations in vapour density to be small, this requires $|T_V - T_S|/T_S \ll 1$. This can be restated in terms of the average temperature gradient and tank radius as $|\nabla T_V|\, R_T/T_S \ll 1$. Let Q_V denote the total amount of heat entering the vapour region through the tank wall. Then, the approximate temperature gradient at the wall due to this heat flux is $Q_V/2\pi R_T(R_T - z_F)k_V$. Thus, in order for temperature variations to be relatively small, it is necessary that

$$\frac{Q_V}{2\pi(R_T - z_F)k_V T_S} \ll 1. \tag{2.19}$$

It is also necessary for the interfacial temperature to change by only a small relative amount over the thermal-diffusion timescale. This can be expressed by the condition

$$\frac{1}{T_S}\frac{\partial T_S}{\partial t}\frac{R_T^2}{\alpha_V} \ll 1. \tag{2.20}$$

When this condition is satisfied, the temperature in the bulk vapour has sufficient time to rise along with the interfacial temperature, preventing any steep thermal boundary layers from forming at the interface. Unfortunately, there is no simple way to test this assumption in advance, because $\partial T_S/\partial t$ is determined by the complete solution, which has yet to be determined. The validity of this assumption will be checked for each solution presented later.

Even though the pressure is spatially uniform, it will change over time if there is some net heat or mass transfer into the vapour region. Let $Q_V = -\int_T \boldsymbol{q}_V \cdot \boldsymbol{n}_T \,\mathrm{d}S$ and $Q_{IV} = \int_I \boldsymbol{q}_V \cdot \boldsymbol{n} \,\mathrm{d}S$ denote the total heat powers coming into the vapour through the tank wall and the vapour side of the interface, respectively. Let $M = \int_I J \,\mathrm{d}S$ be the total rate at which liquid mass is being evaporated. If V is the volume of the vapour region, then the rate at which the total vapour mass changes is given by

$$\frac{\mathrm{d}}{\mathrm{d}t}(\rho_{\mathrm{V}} V) = M. \tag{2.21}$$

If the internal energy of the vapour per unit mass is denoted by e, then the rate at which the total vapour energy changes is given by

$$\frac{\mathrm{d}}{\mathrm{d}t}(\rho_{\mathrm{V}} V e) = Q_{\mathrm{V}} + Q_{\mathrm{IV}} + M\left(e + \frac{p_{\mathrm{V}}}{\rho_{\mathrm{V}}}\right) - p_{\mathrm{V}}\frac{\mathrm{d}V}{\mathrm{d}t}. \tag{2.22}$$

The third term on the right-hand side of (2.22) is the incoming flux of internal energy due to evaporation, the fourth term is the pressure work done by evaporation, and the last term is the pressure work due to volume change. For an ideal gas, the internal energy is solely a function of temperature,

$$e = c_{\mathrm{V}} T, \tag{2.23}$$

where c_{V} is the vapour specific heat at constant volume. The energy required for evaporation is provided by the integrated heat flux difference across the interface (neglecting the very small kinetic energy changes),

$$LM = Q_{\mathrm{IL}} - Q_{\mathrm{IV}}, \tag{2.24}$$

where $Q_{\mathrm{IL}} = \int_{\mathrm{I}} \boldsymbol{q}_{\mathrm{L}} \cdot \boldsymbol{n}\,\mathrm{d}S$ is the total integrated heat flux on the liquid side of the interface.

Both the total tank volume V_{T} and the total mass inside the tank are fixed, so the change in vapour mass must equal the change in liquid mass,

$$\frac{\mathrm{d}}{\mathrm{d}t}(\rho_{\mathrm{V}} V) = \frac{\mathrm{d}}{\mathrm{d}t}[\rho_{\mathrm{L}}(V - V_{\mathrm{T}})] = \frac{\mathrm{d}}{\mathrm{d}t}(\rho_{\mathrm{L}} V). \tag{2.25}$$

The solution of these equations is outlined in the Appendix and results in a single nonlinear evolution equation satisfied by p_{V},

$$\frac{\mathrm{d}p_{\mathrm{V}}}{\mathrm{d}t} = F(Q_{\mathrm{V}} + Q_{\mathrm{IL}}), \tag{2.26}$$

where F is given by

$$F(p_{\mathrm{V}}) = \frac{L}{V}\left\{c_{\mathrm{V}} T_{\mathrm{S}} + \left(\frac{Lm}{R_{\mathrm{G}} T_{\mathrm{S}}} - 1\right)\frac{\rho_{\mathrm{L}}}{\rho_{\mathrm{L}} - \rho_{\mathrm{S}}}\left[L - p_{\mathrm{V}}\left(\frac{1}{\rho_{\mathrm{S}}} - \frac{1}{\rho_{\mathrm{L}}}\right)\right]\right\}^{-1}, \tag{2.27}$$

where ρ_{S} is the vapour density evaluated at the saturation temperature corresponding to p_{V}, and V can be written as a function of ρ_{S} according to (A 2). The liquid-side heat power Q_{IL} depends on p_{V} because of the interfacial boundary condition $T_{\mathrm{I}} = T_{\mathrm{S}}(p_{\mathrm{V}})$. Thus, the rate of change of vapour pressure depends on the liquid heat flux, but the liquid heat flux, in turn, depends on the vapour pressure. This is the manner by which the liquid and vapour regions are coupled together.

If the vapour pressure does not change much from its initial value over the time period of interest, then F can be replaced by its constant initial value F_0 evaluated at the initial pressure p_0. This is true for the cases that will be examined in this paper, and replacing F by F_0 yields nearly identical results. If Q_{V} and Q_{IL} were constant, then (2.26) could be integrated immediately with the result that p_{V} would increase linearly with time. This agrees with the upcoming numerical results after the spatial temperature distribution in the liquid has reached its static configuration since

Q_{IL} approaches a constant. For earlier times, the transient nature of Q_{IL} requires a non-trivial solution of (2.26).

Not all of the terms in (2.27) are equally important. For hydrogen at its normal boiling point, the vapour–liquid density ratio is small, $\rho_{\mathrm{V}}/\rho_{\mathrm{L}} \ll 1$, and the specific heat and pressure work terms are of lesser significance. By retaining only the most important term,

$$F \approx \frac{R_{\mathrm{G}} T_{\mathrm{S}}}{L V m}. \tag{2.28}$$

This shows that the vapour pressure will increase more slowly as the latent heat L or the vapour volume V increases. This agrees with physical intuition since a larger latent heat means the same heat flux will evaporate less liquid, and the dependence on V is what we would expect from the ideal gas law.

2.5. *Thermodynamic model of the entire tank*

Before solving this complicated problem, it is useful to consider the simpler limiting case that would be obtained by assuming that the liquid temperature is also nearly uniform, $T_{\mathrm{L}} \approx T_{\mathrm{V}} \approx T_{\mathrm{S}}$. This would require $(T_{\mathrm{L}} - T_{\mathrm{S}})/T_{\mathrm{S}} \approx \nabla T_{\mathrm{L}} R_{\mathrm{T}}/T_{\mathrm{S}} \ll 1$. Since the temperature gradient near the heater is approximately $q_{\mathrm{H}}/k_{\mathrm{L}}$, this requires $q_{\mathrm{H}} R_{\mathrm{T}}/T_{\mathrm{S}} k_{\mathrm{L}} \ll 1$. In addition, the interfacial temperature cannot be changing too fast. As in the vapour, this requires $\partial T_{\mathrm{S}}/\partial t \ll \alpha_{\mathrm{L}} T_{\mathrm{S}}/R_{\mathrm{T}}^2$.

If these assumptions are valid, the boundary conditions at the free surface can be ignored because mass, momentum and energy are conserved across the interface (it does not change the total amount in the system). It is also assumed that any kinetic energy within the tank is negligible with respect to the internal energy. Equating the total change in internal energy to the energy flux coming in through the boundaries results in

$$\begin{aligned}\frac{\mathrm{d}}{\mathrm{d}t}\left[\rho_{\mathrm{S}} V c_{\mathrm{V}} T_{\mathrm{S}} + \rho_{\mathrm{L}} (V_{\mathrm{T}} - V) c_{\mathrm{L}} T_{\mathrm{S}}\right] &= Q_{\mathrm{T}} + \rho_{\mathrm{L}} A_{\mathrm{J}} w_{\mathrm{J}} c_{\mathrm{L}} (T_{\mathrm{J}} - T_{\mathrm{S}}) \\ &\quad + (p_{\mathrm{J}} - p_{\mathrm{O}}) w_{\mathrm{J}} A_{\mathrm{J}} + \rho_{\mathrm{L}} A_{\mathrm{J}} w_{\mathrm{J}}^3 \left(1 - \frac{1}{2}\frac{A_{\mathrm{J}}^2}{A_{\mathrm{O}}^2}\right),\end{aligned} \tag{2.29}$$

where Q_{T} is the total heat passing through the tank walls, p_{J} is the pressure at the jet nozzle, p_{O} is the pressure at the outlet and A_{J} and A_{O} are the areas of the jet inlet and outlet, respectively. The additional terms on the right-hand side of this equation (in left to right order) represent differences in the convected internal energy, 'flow work' due to pressure forces and kinetic energy between the inlet and outlet regions. Conservation of total mass in the tank requires

$$\frac{\mathrm{d}}{\mathrm{d}t}\left[\rho_{\mathrm{S}} V + \rho_{\mathrm{L}} (V_{\mathrm{T}} - V)\right] = 0. \tag{2.30}$$

It can be shown that the sum of the flow-work and kinetic-energy terms is equal to the total integral of the viscous-dissipation term inside the tank, and this is normally negligible for most situations. Even so, they are included here for completeness. The exact manner by which the energy is dissipated is not consequential for this simple analysis; only the total integrated value is relevant. In fact, this expression holds even if the jet becomes turbulent inside the tank. In that case, the directed kinetic energy of the jet is transformed into the random kinetic energy of turbulent eddies, which is eventually transformed by viscous dissipation into random molecular motion. This increases the internal energy of the system and is accounted for by (2.30).

Note that the pressure difference $p_\mathrm{J} - p_\mathrm{O}$ will be of the order of the dynamic pressure scale since the constant thermodynamic pressures will cancel. This is the pressure difference required to maintain the jet and is nearly equal to the pressure difference across the external pump.

In order to keep the temperature from rising, it is necessary to pick the characteristics of the jet so that

$$\rho_\mathrm{L} A_\mathrm{J} w_\mathrm{J} c_\mathrm{L} (T_\mathrm{J} - T_\mathrm{S}) + (p_\mathrm{J} - p_\mathrm{O}) w_\mathrm{J} A_\mathrm{J} + \rho_\mathrm{L} A_\mathrm{J} w_\mathrm{J}^3 \left(1 - \frac{1}{2}\frac{A_\mathrm{J}^2}{A_\mathrm{O}^2}\right) = -Q_\mathrm{T}. \tag{2.31}$$

This can be satisfied by choosing many combinations of the jet parameters. For example, the jet diameter and flow rate could be fixed and the jet temperature varied, or the jet temperature and diameter could be fixed and the flow rate varied. It is probably better to fix the temperature and vary the flow rate because a higher flow rate will also tend to mix the liquid, making the uniform temperature approximation even more valid. However, as the flow rate increases, so does the amount of kinetic energy dissipated as heat in the liquid. This always works against the desired cooling effect of the jet.

If the assumptions leading up to (2.29) are valid, then it is easy to control the tank pressure. In a realistic situation, it is unlikely that the incoming heat Q_T is known, *a priori*. It depends on the environment surrounding the tank, and that may change from time to time. For example, if the tank is on Mars, it may vary because the amount of solar radiation changes significantly between night and day. However, it can be determined by measuring the temperature rise (or pressure rise since the two are related by the saturation condition) and then using this to compute Q_T from (2.29). Once Q_T is known, a jet with characteristics satisfying (2.31) can be used to cancel the heating effect of Q_T exactly. If there is still some temperature rise even when the jet is being used, then this indicates that Q_T is changing with time, but it can still be computed at each instant from (2.29). With each new value of Q_T, the jet parameters can be adjusted accordingly.

2.6. *Dimensionless parameters*

It is possible to write the governing equations in dimensionless form by defining the length scale R_T, velocity scale w_J, pressure scale $\rho_\mathrm{L} w_\mathrm{J}^2$, time scale $R_\mathrm{T}/w_\mathrm{J}$, temperature scale $q_\mathrm{H} R_\mathrm{T}/k_\mathrm{L}$ and mass-flux scale q_H/L. This results in at least 20 independent dimensionless parameters, but not all of them are equally important for the present analysis. For this reason, only the most important dimensionless parameters will be discussed here, and a more thorough dimensional analysis will be left for future work.

The dimensionless liquid equations depend only on three dimensionless parameters: the Grashof number $Gr = g\beta_\mathrm{L} q_\mathrm{H} R_\mathrm{T}^4/(k_\mathrm{L} \nu_\mathrm{L}^2)$, the Reynolds number $Re = R_\mathrm{T} w_\mathrm{J}/\nu_\mathrm{L}$ and the Prandtl number $Pr = \nu_\mathrm{L}/\alpha_\mathrm{L}$. When $Gr/Re^2 = O(1)$, the mixing jet will become just as important as natural convection. For the present case, $Gr/Re^2 = 3.38$, so it is expected that the jet will have some effect on the temperature distribution. The numerical results that follow will show that the jet interacts with the flow due to natural convection in a non-trivial manner, but neither one completely dominates the bulk mixing behaviour. A more comprehensive parametric analysis is required to determine the behaviour over a wider range of parameters. When there is no jet, the jet velocity scale can be replaced by the viscous velocity scale $\nu_\mathrm{L}/R_\mathrm{T}$. Then, the Reynolds number as defined above simplifies to $Re = 1$ since the fluid velocity is no longer an independent parameter, and only two dimensionless parameters remain to describe the bulk liquid motion.

The three parameters that are traditionally used to characterize the interaction of the jet with the free surface are the Weber number $We = \rho_L w_J^2 d_J^2/(8\sigma R_T)$, the Bond number $Bo = g\rho_L d_J^2/(4\sigma)$ and the jet Reynolds number $Re_J = d_J w_J/(2\nu_L) = d_J/(2R_T)Re$. The Weber number is the ratio of the jet's inertia force to the surface tension force, and the Bond number is the ratio of the gravitational force to the surface-tension force. The jet Reynolds number is the ratio of inertial to viscous forces and is a guiding parameter to determine whether the jet is laminar or turbulent. A general rule deduced from the experimental results of Aydelott (1983) is that the jet is laminar if $Re_J < 450$, a mixture of laminar and turbulent if $450 < Re_J < 1500$ and fully turbulent if $Re_J > 1500$. In that same paper, the deflection of the free surface is correlated to the Bond and Weber numbers. The general trend is that the free-surface deflection is directly proportional to the Weber number but inversely proportional to the Bond number.

The values of these dimensionless parameters for the cases considered here are given in table 2 using the properties in table 1. The jet is expected to be laminar since $Re_J = 266 < 450$. The Weber number is also extremely small and the Bond number is moderately large, so there should not be any significant deflection of the free surface. This is verified by the subsequent numerical results.

3. Numerical solution method

The liquid equations are solved by using a modified version of the commercial Galerkin finite-element code FIDAP (Engelman & Sani 1984). The temperature and velocity fields are discretized using 9-node quadratic elements, and the pressure is discretized using a linear discontinuous approximation (the three pressure unknowns per element are the coefficients of the linear polynomial approximating the pressure). The position of the free surface is adjusted using a front-tracking approach. The locations of the interior nodes are adjusted using the method of spines. The spatial mesh is refined until grid convergence is achieved, as demonstrated in the next section. The mesh used for all the results in this paper consists of 1 167 091 non-uniformly distributed elements. More elements are concentrated near the free surface and tank walls, because this is where the largest solution gradients are observed.

The implicit backward-Euler method (with a forward-Euler predictor) is used for the time discretization, and the time steps are chosen adaptively by using a method that keeps the relative time truncation error at less than the prescribed tolerance ϵ. Specifically, if $\mathrm{d}t^n$ and $\mathrm{d}t^{n+1}$ are the time increments for time steps n and $n+1$, then at the end of time step n, $\mathrm{d}t^{n+1}$ is computed by $\mathrm{d}t^{n+1} = \mathrm{d}t^n(\epsilon/\|\boldsymbol{d}^{n+1}\|)^{1/2}$, where $\|\boldsymbol{d}^{n+1}\|$ is the L_2 norm of the correction (Gresho, Lee & Sani 1979). At each time step, the resulting nonlinear system of equations is solved using an iterative quasi-Newtonian method (Engelman, Strang & Bathe 1981), and convergence is attained when the relative change in the solution norm is less than the prescribed tolerance 10^{-6}. The Jacobian is updated after every 5 iterations using Broyden's method.

The temperature boundary condition (2.11) can often be confidently replaced by the simpler form $T_I = T_S$ since the departure from equilibrium is small for normal evaporation rates. In the current numerical implementation, this boundary condition is further replaced by a natural boundary condition of the form

$$\boldsymbol{q}_L \cdot \boldsymbol{n} = h\,(T_I - T_S)\,, \tag{3.1}$$

where h is an artificial heat transfer coefficient chosen large enough so that the desired boundary condition is closely approximated. The reason for using this form is that

Symbol	Description	Value
ρ_V	Vapour density	$0.00133\,\mathrm{g\,cm^{-3}}$
ρ_L	Liquid density	$0.07047\,\mathrm{g\,cm^{-3}}$
k_V	Vapour thermal conductivity	$4885\,\mathrm{erg\,cm^{-1}\,s^{-1}\,K^{-1}}$
k_L	Liquid thermal conductivity	$12\,440\,\mathrm{erg\,cm^{-1}\,s^{-1}\,K^{-1}}$
μ_V	Vapour dynamic viscosity	$3.207 \times 10^{-5}\,\mathrm{g\,cm^{-1}\,s^{-1}}$
μ_L	Liquid dynamic viscosity	$1.327 \times 10^{-4}\,\mathrm{g\,cm^{-1}\,s^{-1}}$
c_V	Vapour specific heat (at constant volume)	$1.012 \times 10^{8}\,\mathrm{erg\,K^{-1}\,g^{-1}}$
c_L	Liquid specific heat (at constant pressure)	$9.7 \times 10^{7}\,\mathrm{erg\,K^{-1}\,g^{-1}}$
α_V	Vapour thermal diffusivity	$0.0256\,\mathrm{cm^2\,s^{-1}}$
α_L	Liquid thermal diffusivity	$0.00182\,\mathrm{cm^2\,s^{-1}}$
β_L	Liquid thermal expansion coefficient	$0.0175\,\mathrm{K^{-1}}$
a	Accommodation coefficient	1.0
σ	Surface tension	$1.93\,\mathrm{dyn\,cm^{-1}}$
L	Latent heat of vaporization	$4.456 \times 10^{9}\,\mathrm{erg\,g^{-1}}$
m	Molar mass	$2.0\,\mathrm{g\,mol^{-1}}$
T_B	Normal boiling temperature	20.27 K
p_B	Normal saturation pressure	$1.014 \times 10^{6}\,\mathrm{dyn\,cm^{-2}}$ (1.0 atm)
T_C	Critical point temperature	32.98 K
p_C	Critical point pressure	$1.2927 \times 10^{7}\,\mathrm{dyn\,cm^{-2}}$ (1.2927×10^{6} Pa)
R_T	Tank radius	5.0 cm
z_F	Fill level	0.0 cm
z_T	Position of heater top	−1.0 cm
z_B	Position of heater bottom	−3.0 cm
d_J	Jet diameter	1.0 cm
d_O	Outlet diameter	2.0 cm
d_N	Jet nozzle diameter	1.2 cm
q_H	Heater heat flux (liquid-heating case)	$100\,\mathrm{erg\,cm^{-2}\,s^{-1}}$ ($0.01\,\mathrm{mW\,cm^{-2}}$)
Q_T	Total heat power input	$6283\,\mathrm{erg\,s^{-1}}$ (0.6283 mW)
w_J	Average jet velocity	$1.0\,\mathrm{cm\,s^{-1}}$
T_J	Inlet jet temperature	20.0 K
g	Acceleration due to gravity on Earth	$981\,\mathrm{cm\,s^{-1}}$
R_G	Ideal gas constant	$8.31 \times 10^{7}\,\mathrm{erg\,K^{-1}\,mol^{-1}}$

TABLE 1. Some material properties of hydrogen and other parameters at the normal boiling point (T_B, p_B).

Parameter	Description	Definition	Value
Gr	Grashof number	$g\beta_L q_H R_T^4/k_L \nu_L^2$	2.4×10^{7}
Re	Tank Reynolds number	$R_T w_J/\nu_L$	2660
Pr	Prandtl number	ν_L/α_L	1.03
We	Weber number	$\rho_L w_J^2 d_J^2/8\sigma R_T$	9.13×10^{-4}
Bo	Bond number	$g\rho_L d_J^2/4\sigma$	8.95
Re_J	Jet Reynolds number	$d_J w_J/2\nu_L$	266

TABLE 2. The most important dimensionless parameters and their numerical values for the present cases.

it also provides a more accurate method for computing the liquid-side interfacial heat flux that avoids having to compute the temperature gradient explicitly. This interfacial heat flux is required by the lumped vapour model in order to determine the vapour pressure rise. The particular value of h is chosen by trial and error to be large enough so that $T_I - T_S$ is much less than any other temperature difference within the liquid (in order to approximate the desired boundary condition), but is also small enough so that the heat flux can be computed by (3.1) despite numerical error. Using the dimensional scales presented in the last section, a sufficient condition for the first requirement is that $k_L/R_T h \ll 1$. The particular value $h = 1.6 \times 10^7 \,\mathrm{erg\,cm^{-2}\,s^{-1}\,K^{-1}}$ was found to satisfy this condition ($k_L/R_T h = 1.6 \times 10^{-4} \ll 1$), but is still small enough so that the heat flux could be accurately computed. This approach is similar to using a non-zero value for κ in (2.11). In fact, if the vapour-side heat flux is neglected in (2.6), then this is equivalent to picking the value $\kappa = L/h$. This method was found to be more accurate and reliable than specifically setting $T_I = T_S$ at the interface and then trying to compute the heat flux by calculating the thermal gradient directly.

The time-dependent saturation temperature T_S appearing in (3.1) is determined by simultaneously solving (2.26) along with the finite-element equations at each time step. This equation is also solved using backward-Euler and Newton's method, but it uses the integrated heat flux from the previous time step because of certain complications in the numerical implementation. Unfortunately, this semi-implicit approach requires smaller time steps than for a fully implicit approach.

4. Results

The solution is obtained for three different tank-wall heat distributions: localized heating in the liquid, direct heating of the vapour and uniform heating over the entire tank wall. The total heat power input is the same for each case and equal to $Q_T = 0.628319\,\mathrm{mW}$. These are motivated by the experiments of Aydelott (1967). In the liquid-heating case, a uniform heat flux of $0.01\,\mathrm{mW\,cm^{-2}}$ is applied over just the heater surface area. The remainder of the tank wall is perfectly insulated. In the uniform-heating case, the heat is distributed evenly over the entire tank surface. For the vapour-heating case, it is released only within the vapour region. For each of these cases, the solution is obtained both with and without a jet. When there is a jet, its speed is $1.0\,\mathrm{cm\,s^{-1}}$ and its temperature is 20 K. The tank is initially half-filled ($z_F = 0$) with liquid hydrogen that is in equilibrium with its saturated vapour at a temperature of 20 K. The other parameters and material properties are given in table 1.

The rate of pressure rise for the liquid-heating case is shown in figure 2 for three different meshes and three values of ϵ. The solution is nearly identical as the number of elements is increased, but there are some noticeable changes as the time tolerance is varied. The value $\epsilon = 0.0001$ provides a suitable compromise between accuracy and efficiency and is used along with the maximum number of elements for all of the results presented here. The approximate computation time for each case varied between 13 and 30 cpu hours running on an SGI Origin 2000 with a single 195 MHz IP27 processor and 512 MB of memory.

The change in vapour pressure up to $t = 7200\,\mathrm{s}$ is shown in figure 3 (*a*) when there is no mixing jet. Also shown is the thermodynamic pressure rise predicted by (2.29). The corresponding saturation temperatures are shown in figure 4 (*a*, *b*). Eventually, the rate of pressure rise is the same for each heat distribution and nearly equal to that predicted by thermodynamics, although there are significant differences for early

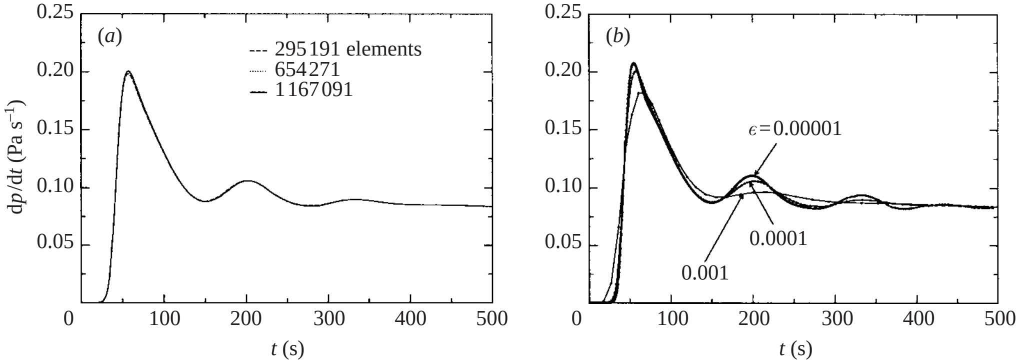

FIGURE 2. The rate at which the vapour pressure rises in the liquid-heating case for three different meshes and three different choices of the maximum time truncation error ϵ. In (*a*), $\epsilon = 0.0001$, and in (*b*) the number of elements is fixed to 1 167 091. The oscillations become more pronounced as ϵ is decreased. The remaining results in this paper use 1 167 091 elements and $\epsilon = 0.0001$.

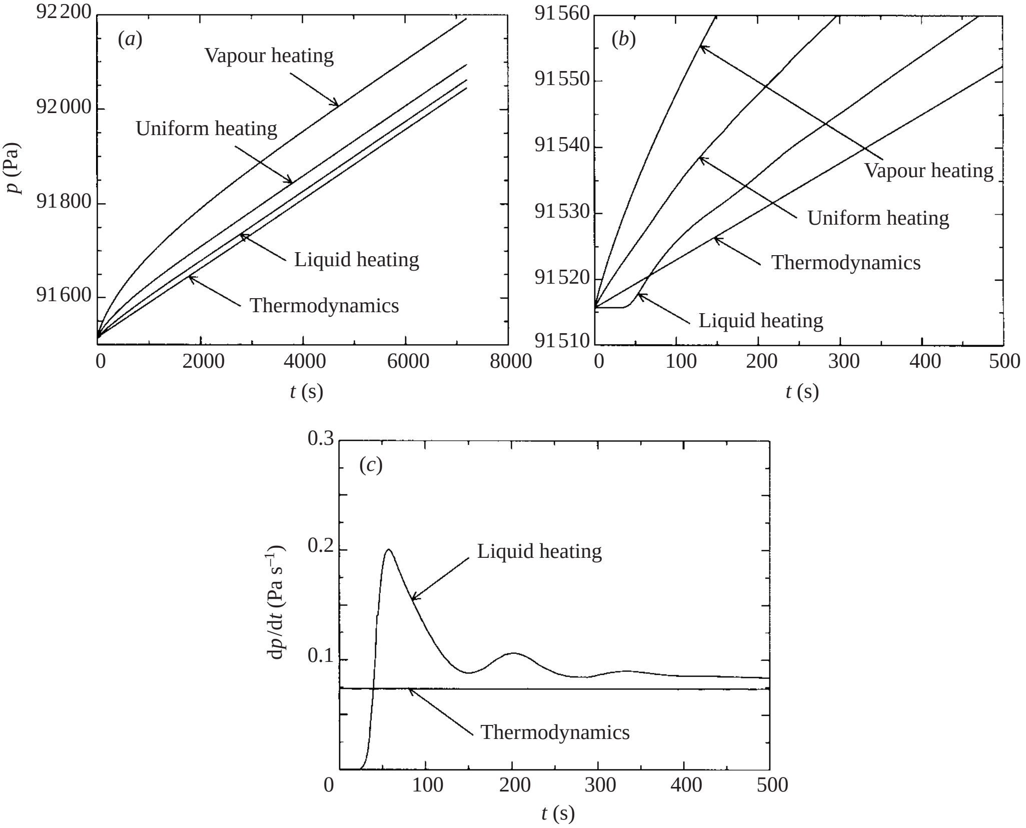

FIGURE 3. (*a*, *b*) Vapour pressure for three different tank-wall heat distributions when there is no jet. The slope of the pressure curve is shown in (*c*) for the liquid-heating case only. The total heat power input is 0.6283185 mW.

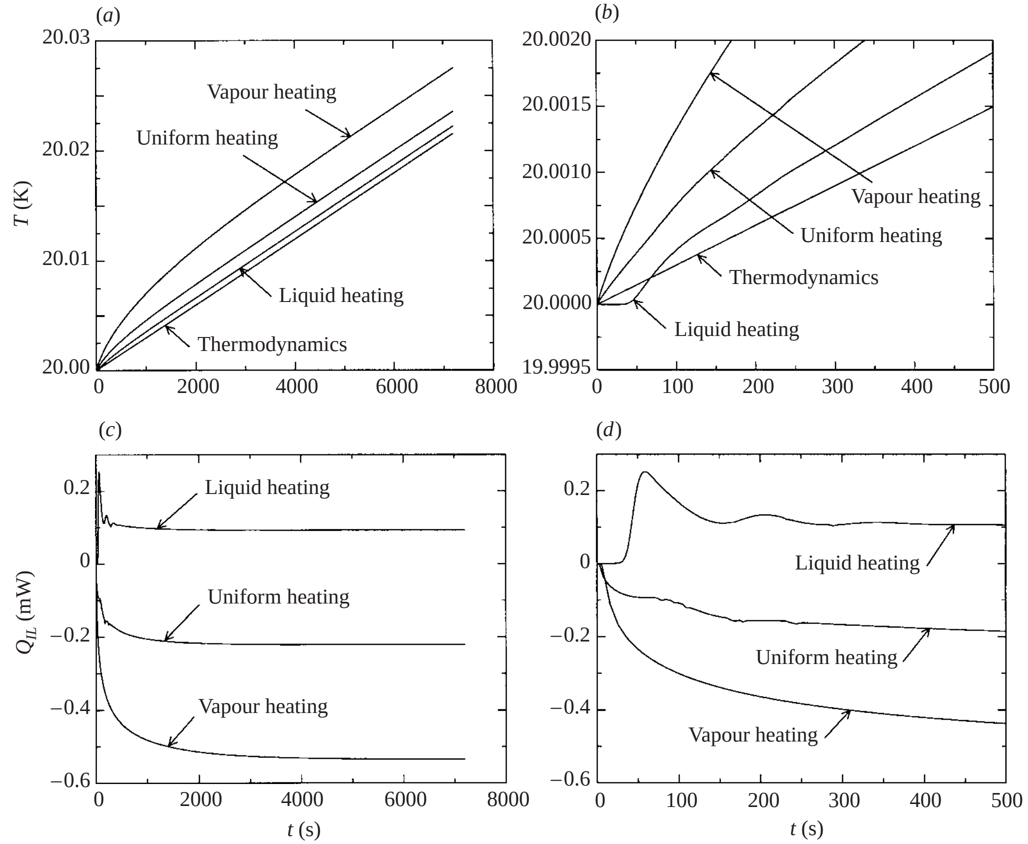

FIGURE 4. (*a*, *b*) Vapour temperature and (*c*, *d*) interfacial heat power for three different tank-wall heat distributions when there is no jet. The total heat power input is 0.6283185 mW.

times as shown in figure 3(*b*). The liquid-heating case most closely follows thermodynamics because it exhibits the most convective mixing, which promotes a more uniform temperature distribution. However, for earlier times, the slope of the pressure curve exhibits oscillations as shown in figure 3(*c*). This can be attributed to a coupling between the buoyancy force and convective cooling as will be explained later. The curve that deviates most from thermodynamics is, not surprisingly, the vapour-heating case because heating from above is a thermally stable situation that minimizes convection in the liquid. In that case, all of the heat enters the liquid primarily through a diffusive boundary layer at the liquid–vapour interface, and this is slower than convective mixing. The uniform-heating case lies between these two extremes since the total heat input is divided evenly between the liquid and vapour regions.

The total interfacial heat flow Q_{IL}, integrated over the entire liquid–vapour interface, is shown in figure 4(*c*, *d*). Part of this energy is used to evaporate more liquid, and part of it is used to heat the existing vapour. After an initial transient, Q_{IL} seems to be approaching a constant value, which is consistent with the observation that the slope of the pressure curve is also approaching a constant value since the two are related by (2.26).

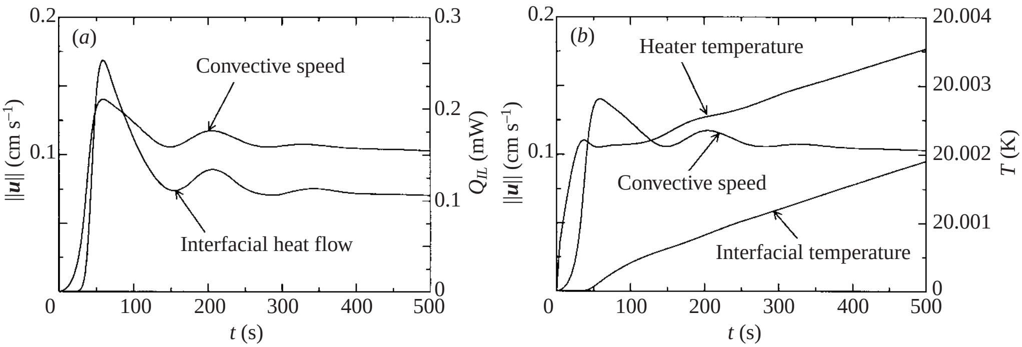

FIGURE 5. The effect of convection on the total interfacial heat flow is shown in (*a*). The heater temperature, interfacial temperature and convective speed for the liquid-heating case are compared in (*b*). The heater temperature is measured at a depth of 1.1 cm beneath the interface (location of maximum temperature), and the convective speed is measured at a point on the interface that is 3.8 cm from the centre of the tank (location of maximum velocity). The oscillations result from a coupling between the buoyancy force and convective cooling.

The fact that the interfacial heat flux is approaching a constant value suggests that the spatial temperature distribution in the liquid is approaching a static configuration even though the average temperature is still increasing. This happens because the time scale for thermal diffusion in the liquid is much shorter than the time scale for changes in the interfacial temperature, $\partial T_S/\partial t \ll \alpha_L T_S/R_T^2$. Thus, after an initial transient, the energy coming in through the tank wall is divided between the energy used to raise the average liquid temperature and that which goes into the vapour region, both of which assume constant values when the static configuration is achieved. This is the same assumption used to derive the thermodynamic model of the entire tank, and this is the reason why the final rate of pressure rise agrees so well with thermodynamics.

The final value of Q_{IL} is 0.092832 mW for the liquid-heating case, −0.221314 mW for the uniform-heating case and −0.535256 mW for the vapour-heating case. In the uniform-heating case, the amount of heat that is added directly to the vapour is 0.314159 mW. Thus, the total amount of heat that remains in the vapour is equal to this amount plus the interfacial heat power, which is negative in this case, i.e. $0.314159\,\mathrm{mW} - 0.221314\,\mathrm{mW} = 0.092845\,\mathrm{mW}$. Similarly, the total amount of heat that remains in the vapour for the vapour-heating case is equal to $0.628319\,\mathrm{mW} - 0.535256\,\mathrm{mW} = 0.093062\,\mathrm{mW}$. Thus, in all three cases, the interfacial heat power adjusts itself so that the same amount of heat goes into the vapour. This has to be true since the slope of each pressure curve agrees with thermodynamics, and this slope is proportional to the total amount of heat going into the vapour. This excellent agreement among the cases (to within two to three significant digits) is also a good indication of the accuracy of the model and of the method used to compute the interfacial heat flux.

The oscillations in Q_{IL} and $\mathrm{d}p/\mathrm{d}t$ for early times are a direct result of oscillations in the convective speed near the interface as shown in figure 5(*a*). The oscillations in the convective speed can be understood by examining figure 5(*b*). The buoyancy force is essentially proportional to the difference between the heater and interfacial temperatures. Fluid near the heater accelerates as this temperature difference increases. However, as the convective speed increases, it brings in cooler fluid from the centre of the tank, reducing this temperature difference. This cycle repeats for a while until the

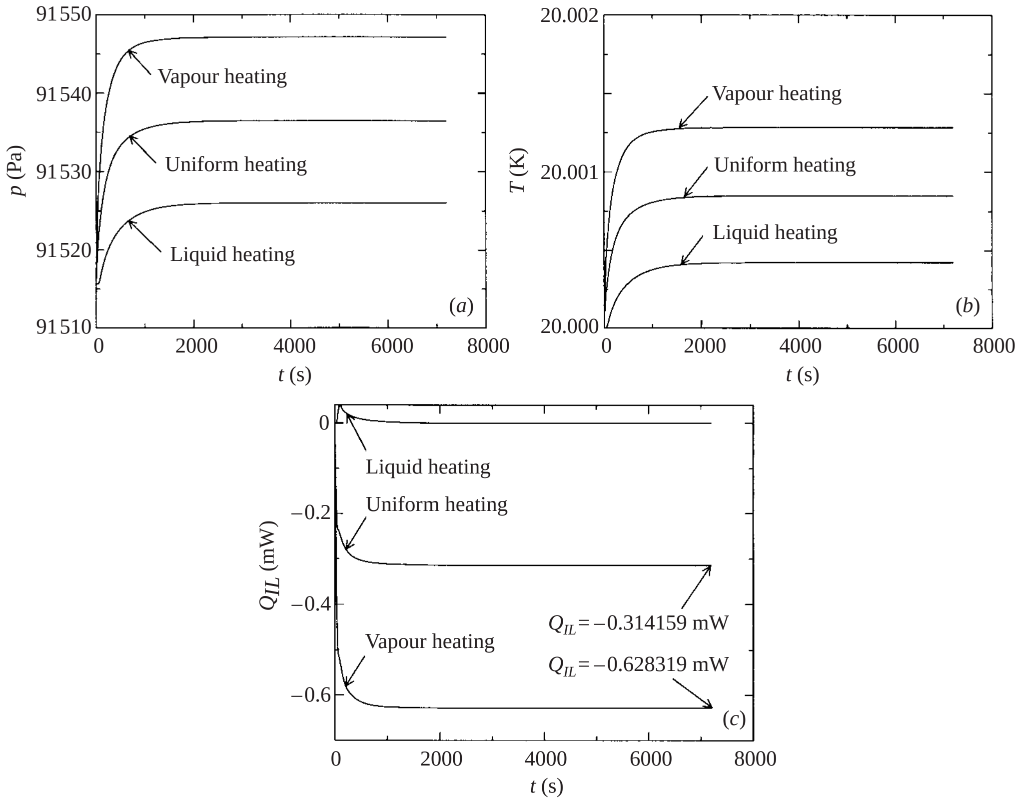

FIGURE 6. (*a*) Vapour pressure, (*b*) vapour temperature and (*c*) interfacial heat flow for the three different tank-wall heat distributions when the jet speed is $1\,\mathrm{cm\,s^{-1}}$ and its temperature is 20 K. The total heat power input for each case is 0.6283185 mW.

temperature difference between the heater and the interface approaches a constant value.

The results shown in figure 6 are for the same cases as before except that now a jet of liquid is forced in from the bottom of the tank with a temperature of 20 K and an average speed of $1\,\mathrm{cm\,s^{-1}}$. The vapour pressure now approaches a constant as the cooling effect of the jet balances the incoming heat. The time required to reach this steady state is about the same for all cases because it depends primarily on how long it takes for the jet to reach and spread across the free surface.

In all of these jet cases, the value of Q_{IL} is the exact negative of the amount of heat that is being added directly into the vapour region so that the net heat input into the vapour region is zero. This has to be true since, otherwise, the temperature and pressure of the vapour would be changing and the solution would not have yet reached a steady state. Measurements of the liquid-side interfacial heat power show that $Q_{\mathrm{IL}} = 0$ for the liquid heating case, $Q_{\mathrm{IL}} = -0.314159\,\mathrm{mW}$ for the uniform-heating case and $Q_{\mathrm{IL}} = -0.628319\,\mathrm{mW}$ for the vapour-heating case. The exact (to within six significant digits) agreement between the heat input and what is actually measured at the interface is another good indication of the accuracy of the model and of the method used to compute the interfacial heat flux.

The final vapour temperature is quite different for each case in figure 6(*b*). The difference between the final temperature and the initial temperature for the

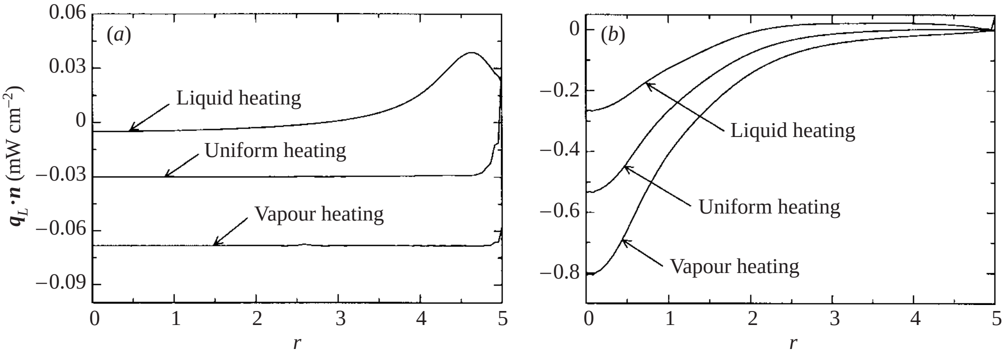

FIGURE 7. Local heat flux on the liquid side of the interface (*a*) with no jet and (*b*) with a jet.

vapour-heating case is almost three times larger than for the liquid-heating case even though the total heat input is the same. This result cannot be predicted by using purely thermodynamic considerations, because such an analysis predicts a single final temperature that depends solely on the total heat power input and not on how this heat is distributed over the boundary. In fact, according to the thermodynamic model (2.31), the final vapour temperature corresponding to a jet with the indicated characteristics should be approximately 20.00117 K (the pressure-work and kinetic-energy terms were negligible for this case). One of the assumptions leading up to (2.31) is that the temperature is the same everywhere in the tank and equal to the vapour temperature. However, this is not the case as the numerical results indicate. It is worth noting that the average liquid temperature over the outlet surface is different from the vapour temperature and equal to 20.001121 K in the liquid heating case, 20.001129 K in the uniform-heating case and 20.001128 K in the vapour-heating case. Interestingly, these temperatures are much closer to the predicted value given by (2.31). Thus, if the lumped analysis for the entire vapour and liquid regions were based on the outlet temperature instead of the saturation temperature, its predictions would be more accurate. This is because the difference between the inlet and outlet temperatures more closely characterizes the amount of energy actually being removed by the jet.

A plot of the local heat flux on the liquid side of the free surface is shown in figure 7(*a*) for those cases without a jet and in figure 7(*b*) for those cases with a jet. When there is no jet, the heat flux reaches a maximum at some interior position for the liquid heating case because this is where the hottest fluid convected from the heater reaches the free surface. The maximum occurs at the wall for the other cases.

In the uniform-heating case, there is a potential singularity in the heat flux at the wall because the temperature along the free surface is nearly forced to be a constant at the same time that a positive heat flux is prescribed at the wall. This forces the liquid at the wall to be hotter than the surrounding liquid, even at a point that is infinitesimally close to the free surface. This leads to a singularity in the interfacial heat flux unless the temperature of the free surface is not constrained to be constant there. This would be the case if a non-zero value of κ were used in the temperature boundary condition (2.11). However, as mentioned in § 3, a non-zero value for κ is effectively obtained by using a finite value for h in (3.1). Removing this singularity is another reason for using this natural boundary condition. This singularity could also be suppressed by giving the wall some finite thickness and then solving for the temperature field inside the wall.

When the jet is used, the heat flux has a minimum value at the centre of the tank where the jet strikes the free surface. The heat flux is negative near the centre because heat is being removed by the jet. In the liquid-heating case, the heat being removed from the vapour region must be equal to the heat being released by vapour that is condensing at the free surface. Near the wall, the heat flux becomes positive, resulting in local evaporation. Thus, there are localized regions of evaporation and condensation at the interface, but they exactly cancel each other so that the net mass transfer into the vapour region is zero. There is a steady flow of vapour from regions of evaporation to regions of condensation.

There is also some mass flow within the liquid due to phase change, but this flow is negligible compared to the flow created by natural convection because the rate of phase change is so small. For example, the heat flux at the centre of the tank for the vapour-heating case with a jet is about $-0.8\,\mathrm{mW\,cm^{-2}}$. According to the interfacial energy balance given by (2.6), this corresponds to a maximum condensation rate of $J = -1.8 \times 10^{-7}\,\mathrm{g\,s^{-1}cm^{-2}}$ assuming all of the heat energy is used for condensation. This leads to a liquid flow speed of only $2.6 \times 10^{-6}\,\mathrm{cm\,s^{-1}}$ using the interfacial mass balance given by (2.4). This is much less than the fluid speed resulting from either natural convection or the jet.

At this point, it would be prudent to check whether the conditions required for the validity of the lumped-vapour approximation are satisfied by the numerical solutions. The first condition given by (2.19) is satisfied because the left-hand side evaluates to 0.002 for the properties given in table 1. The second condition given by (2.20) requires a value for $\partial T_S/\partial t$, and this can be obtained from the solution in figures 4(b) and 6(b). Using the maximum value at time $t = 0$ for the vapour-heating case with no jet, the left-hand side of (2.20) evaluates to about 0.001. Thus, both conditions are satisfied for this particular problem, and the lumped-vapour approximation is valid for the cases considered here.

Contour plots of the final temperature field and streamlines in the liquid at $t = 7200\,\mathrm{s}$ are shown in figure 8 for the liquid-heating case. Although not shown here, the solution at $t = 3600\,\mathrm{s}$ looks identical to the final solution, and it is clear that the spatial structure of the solution has reached a steady state for both the jet and no-jet cases.

When there is no jet, the streamlines indicate that there is a counterclockwise circulation due to natural convection that is primarily confined to the upper half of the tank. Because of this, the temperature of the liquid throughout the top half is nearly uniform despite pronounced thermal stratification in the bottom half. The final maximum convective speed is about $0.0932\,\mathrm{cm\,s^{-1}}$ at a point located on the interface near the heater where the spacing between the streamlines is a minimum. As expected, there is no noticeable deflection of the free surface.

When the jet is used, cooler fluid enters from the bottom of the tank, spreads across the free surface and is deflected downwards forming a clockwise circulation cell where the free surface meets the tank wall. The counterclockwise cell due to natural convection has been forced into the lower half of the tank by the action of this jet. On its way out, the jet fluid rides around this cell and is pushed back towards the centre of the tank where it then turns downward and moves out of the bottom through the outlet. The free surface is deflected slightly at the centre, but that is barely noticeable on this scale.

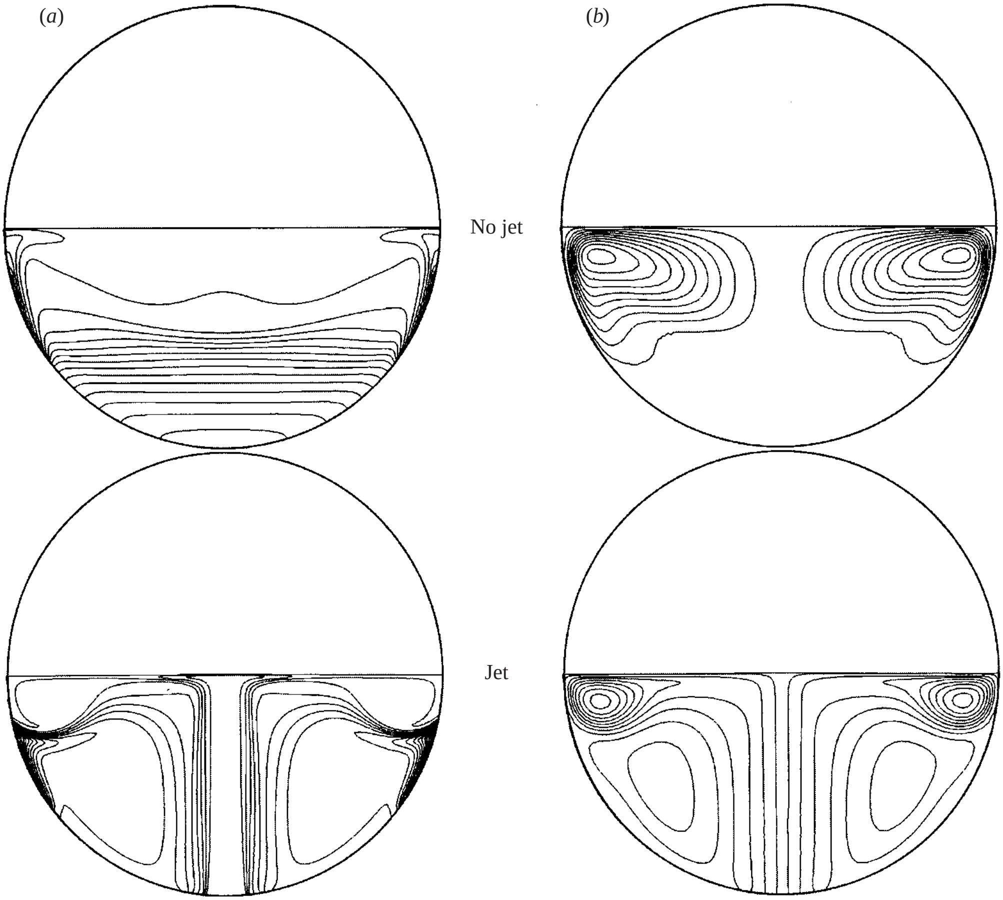

FIGURE 8. (*a*) Temperature contours and (*b*) streamlines at $t = 7200$ s for liquid heating both with and without a jet. The contours are evenly spaced between the minimum and maximum values. The minimum and maximum temperatures are 20.018419 K and 20.023815 K for the no-jet case and 20 K and 20.004278 K for the jet case. The maximum convective velocity for the no-jet case is 0.0932 cm s^{-1}.

The final solution at $t = 7200$ s for the uniform-heating case is shown in figure 9. When there is no jet, there is a thermal boundary layer near the interface owing to the direct heating of the vapour in addition to the thermal boundary layer near the tank wall. There is still a natural-convection cell, but it is weaker and more spread out than before. The maximum speed is 0.0309 cm s^{-1}, and it occurs near the tank wall about halfway down. When the jet is used, the solution looks very similar to the corresponding liquid-heating case.

The final solution for the vapour-heating case is shown in figure 10. A thermal boundary layer initially develops near the interface as the vapour temperature rises, leading to pronounced thermal stratification throughout the liquid. There is only a minimal amount of convection due to a slight radial temperature gradient near the walls caused by specifying an insulated boundary condition on the spherical surface. The magnitude of this convection is much less than for the other cases, only about 0.00497 cm s^{-1}. When the jet is used, the flow field looks like the other cases, but the temperature field is quite different. The temperature changes rapidly around the jet

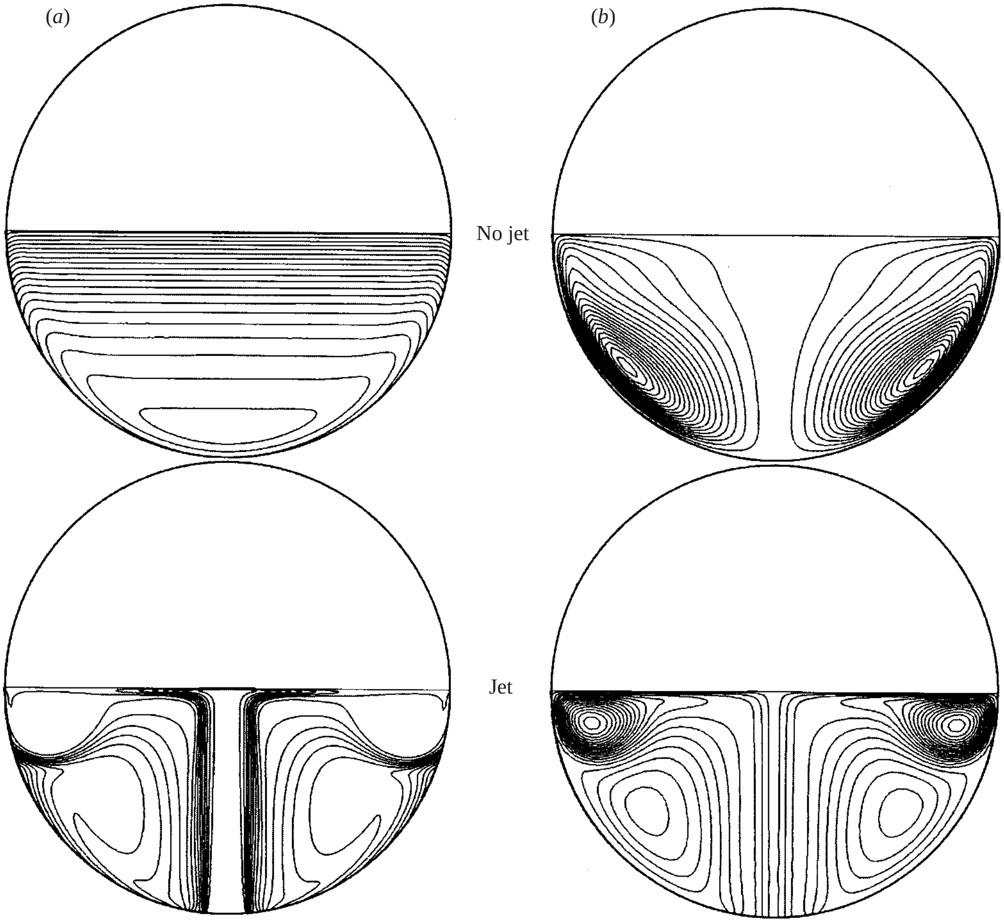

FIGURE 9. (a) Temperature contours and (b) streamlines at $t = 7200$ s for uniform heating both with and without a jet. The contours are evenly spaced between the minimum and maximum values. The minimum and maximum temperatures are 20.019849 K and 20.023583 K for the no-jet case and 20 K and 20.002330 K for the jet case.

and next to the free surface, but it is nearly constant everywhere else because no heat is entering through the tank walls.

By comparing the final temperature contours for the jet cases in figures 8, 9 and 10, we can see why a lumped analysis of the whole system is more inaccurate if it is based on the vapour temperature instead of on the outlet temperature. In the liquid-heating case, much of the heat being added directly to the liquid is absorbed by the jet and exits through the outlet before ever reaching the vapour. This is why the final vapour temperature is lower in the liquid-heating case and why the temperature difference between the vapour and outlet is so large. In the vapour-heating case, all of the heat is added directly to the vapour and is absorbed by the cooler jet right at the free surface. This is why there is little temperature variation elsewhere in the tank, and the outlet temperature is nearly equal to the vapour temperature. In all cases, the average outlet temperature is about the same as that predicted by (2.31). For this reason, if a lumped analysis of the whole tank is preferred, it should be based on the

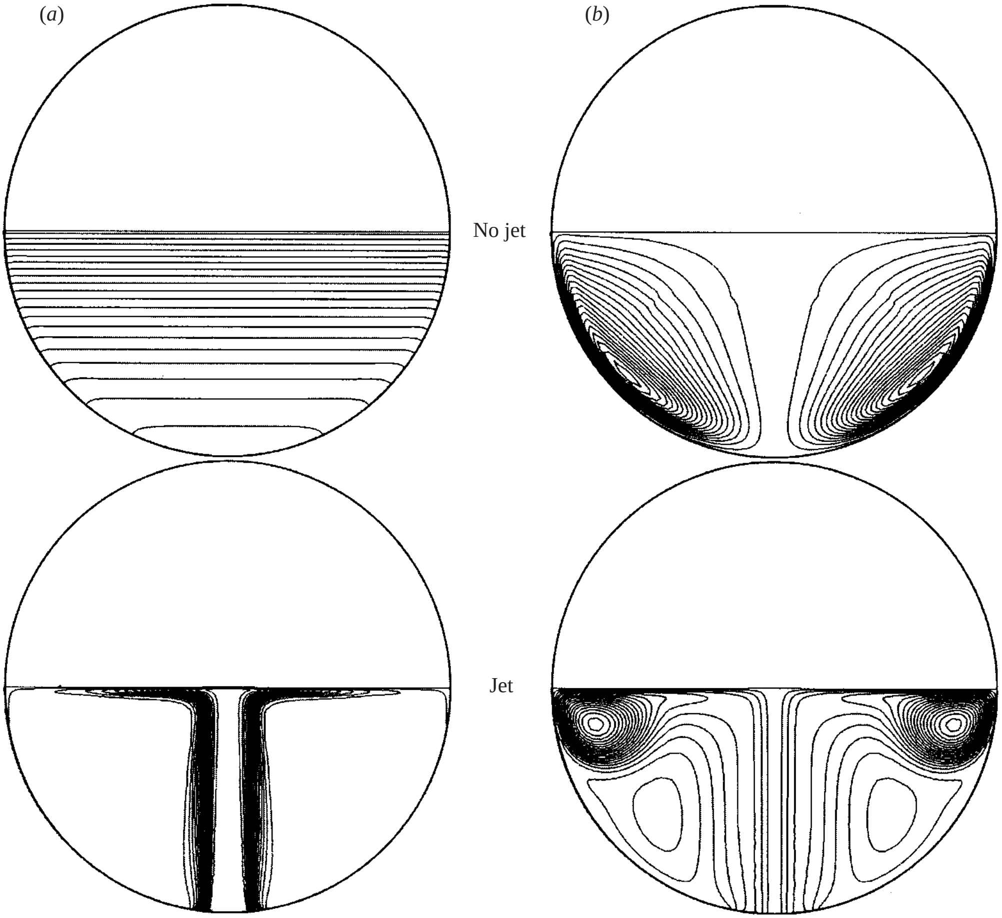

FIGURE 10. (*a*) Temperature contours and (*b*) streamlines at $t = 7200$ s for vapour heating both with and without a jet. The contours are evenly spaced between the minimum and maximum values. The minimum and maximum temperatures are 20.014994 K and 20.027508 K for the no-jet case and 20 K and 20.001284 K for the jet case.

difference between the average liquid temperature at the outlet and the incoming jet temperature.

5. Conclusions

The validity of a thermodynamic treatment of cryogenic storage tanks is tested by comparing with direct numerical solutions for three different tank-wall heating distributions. The complete solution is obtained inside the liquid region, but a lumped approximation is used for the vapour region. The lumped-vapour model accounts for any heat and mass flow across the liquid–vapour interface as well as any heat coming in directly through the tank walls. A liquid jet is sometimes used to mix the liquid and control the tank pressure. The primary objective is to be able to predict the tank pressurization and temperature rise under a number of different scenarios both with and without the mixing jet. Only a ground-based tank is considered here where the liquid is always at the bottom of the tank, but the methods developed here can equally apply to space-based tanks.

For the cases without a jet, it is shown that the final rate at which the vapour pressure rises in a small cryogenic tank is very close to that predicted by thermodynamics, even though the initial transients and final pressures are different. When all of the heat enters through the liquid, natural convection promotes mixing of the fluid and redistributes the heat more evenly. Initially, the vapour pressure rises most slowly in this case because a larger portion of the incoming heat power is used to heat the liquid and less is available for evaporation. Even so, the final pressure in this case is closest to thermodynamic predictions because it exhibits the strongest liquid mixing. At the opposite extreme, if all of the heat is added directly to the vapour, the pressure rises most rapidly at first, and a thermal boundary layer develops on the liquid side of the interface. This is a thermally stable configuration, and the magnitude of convective mixing in the liquid is greatly reduced. Thus, the rate at which heat can leave the vapour is conduction limited and accounts for the rapid initial pressure rise. When the heat is distributed uniformly over the tank surface, the solution lies between these two extremes.

In the liquid-heating case, there is also a curious initial oscillation in the vapour pressure and interfacial heat flux that appears because of a coupling between the buoyancy force and convective cooling. As the heater temperature increases, so does the buoyancy force. This increases the convective speed and brings cooler fluid in near the wall. This cools the heater, which reduces the strength of natural convection and permits the heater temperature to start increasing again. This effect appears to be a rather general consequence of convective heating with a specified wall heat flux, and it should not be limited solely to the context of cryogenic tanks. It would probably be diminished or completely suppressed by specifying the heater temperature instead of the heat flux.

When a liquid jet is used to mix and cool the bulk liquid, the final pressure approaches a constant as the cooling effect of the jet balances the heat input. The time required to reach this steady state is about the same in all cases and depends on the convective time scale of the jet. As before, the final pressure is highest in the vapour-heating case and lowest in the liquid-heating case. At steady state, the total interfacial heat flow exactly balances the amount of heat being added directly to the vapour. This is a necessary condition for there to be a steady state since any net amount of heat added to the vapour would increase its pressure.

One general conclusion that can be surmised from all of these cases is that the final pressure is always highest for the case in which most of the heat is directly added to the vapour, even when the total heat power input is the same. This is true with or without a jet and is a result that cannot be obtained solely from thermodynamics since it depends on the initial transient and on the temperature distribution in the liquid. This may appear, at first glance, to violate thermodynamics since the total heat input is the same, but it does not. If the heat input were to suddenly stop, there would be another final transient after which the temperature and pressure in each case would be the same. In a real cryogenic tank, the process is always transient since there is always some net heat input leaking in through the walls. This is why thermodynamics alone is unable to completely describe these systems. Moreover, the departure from thermodynamics becomes even worse as the tanks become larger. Thus, when designing cryogenic tanks, especially those planned for long-duration space missions, every effort should be made to restrict the amount of heat entering directly into the vapour.

It also follows that the quickest way to reduce the pressure in the tank is to place a cryocooler directly in the vapour. This is because the thermal inertia of the vapour is normally much less than that of the liquid, and so changes in temperature and pressure in the vapour happen more quickly than in the liquid. Thus, even though a cooling jet in the liquid can be used to control the pressure in the tank over the long term, it would be unable to control rapid fluctuations in pressure resulting from sudden changes in heat input to the vapour. Thus, from an idealized point of view, a combination of a cryocooler in the vapour and a jet in the liquid might be the best option.

The general trends predicted by the present model show better agreement with the experimental results of Aydelott (1967) than the two simpler thermodynamic models used in that paper. These were the homogeneous model, where the liquid and vapour are both at the same temperature and pressure, and the surface evaporation model, where all the heat is assumed to go directly into the vapour with the liquid temperature held constant at its initial value. The experiments show that the initial rate of pressure rise is greatest for the vapour-heating case and lowest for the liquid-heating case, in agreement with the present model results. The homogeneous model is able to describe the liquid-heating case and the surface evaporation model agreed with the vapour-heating case, but neither model could describe both scenarios equally well. The approach formulated in the present paper essentially combines these two simpler models into a single unified model with the additional feature that the complete liquid dynamics and free-surface motion are also determined. Unfortunately, it is not possible to compare directly with these experimental results because the applied heat flux was so large as to result in turbulent natural convection, and the present model does not account for turbulence. Nevertheless, it is seen that the general trends predicted herein also seem to hold for the higher heat flux cases. Future work will consider how to best extend the current model to account for turbulence so that more direct comparisons can be made.

The present analysis was performed for a scaled ‘model’ tank being developed in our fluid visualization laboratory. This tank is much smaller than those being proposed for future manned space missions. The scale-up problem poses serious complications. For larger tanks, the lumped-vapour approximation may no longer be valid and the mixing jet may become turbulent. Also, in a space-based tank there could be multiple vapour bubbles surrounded by liquid floating around with no preferred equilibrium position. If a jet is used to mix the liquid, this could push some of the vapour bubbles up against the wall changing the heating mode from one of liquid-heating to one of vapour-heating.

Some insight can be gained about this space-based scenario by considering the ground-based results already obtained. For a space-based tank with completely wetted walls, the pressure would rise slowly as in the liquid-heating case. However, if one of the vapour bubbles were to come into contact with the wall, then the vapour pressure would suddenly rise more rapidly, as in the vapour-heating case. The vapour pressure might behave erratically depending on the dynamic configuration of liquid and vapour. A model of this scenario is currently being developed using the same lumped-vapour approach as described in this paper, but with a more sophisticated treatment of the free surface to account for the complex vapour bubble dynamics.

This work was funded by the National Center for Microgravity Research (NCMR) and the United Space Research Consortium (USRA).

Appendix. Derivation of the lumped-vapour model

First, note that the vapour density is equal to its saturation value,

$$\rho_{\mathrm{V}} = \rho_{\mathrm{S}}(p_{\mathrm{V}}) = \frac{p_{\mathrm{V}} m}{R_{\mathrm{G}} T_{\mathrm{S}}}, \tag{A 1}$$

which only depends on p_{V} since $T_{\mathrm{S}} = T_{\mathrm{S}}(p_{\mathrm{V}})$ is a function of p_{V}. The vapour volume depends on ρ_{S} since (2.25) can be immediately integrated with the result

$$V = V_0 \frac{\rho_{\mathrm{L}} - \rho_{\mathrm{S},0}}{\rho_{\mathrm{L}} - \rho_{\mathrm{S}}} = V_0 \left(1 + \frac{\rho_{\mathrm{S}} - \rho_{\mathrm{S},0}}{\rho_{\mathrm{L}} - \rho_{\mathrm{S}}}\right), \tag{A 2}$$

where V_0 is the initial volume and $\rho_{\mathrm{S},0}$ is the initial density. This shows that the vapour volume will be close to its initial value if the change in vapour density is small compared to the overall density difference between liquid and vapour.

By making use of (2.21), (2.25) is written as

$$\frac{\mathrm{d}V}{\mathrm{d}t} = \frac{M}{\rho_{\mathrm{L}}}, \tag{A 3}$$

and then this is substituted into (2.22). Next, (2.24) is solved for Q_{IV} and substituted into (2.22). The left-hand side of (2.22) is expanded and the relationship for M in (2.21) is used to eliminate Me from both sides of the equation. This all leads to

$$\rho_{\mathrm{S}} V \frac{\mathrm{d}e}{\mathrm{d}t} + M \left[L - p_{\mathrm{V}} \left(\frac{1}{\rho_{\mathrm{S}}} - \frac{1}{\rho_{\mathrm{L}}}\right)\right] = Q_{\mathrm{V}} + Q_{\mathrm{IL}}. \tag{A 4}$$

By substituting $e = c_{\mathrm{V}} T_{\mathrm{S}}$ and the expression for M given by (2.21) into (A 4),

$$\left\{\rho_{\mathrm{S}} V c_{\mathrm{V}} \frac{\partial T_{\mathrm{S}}}{\partial p_{\mathrm{V}}} + \frac{\partial}{\partial p_{\mathrm{V}}}(\rho_{\mathrm{S}} V) \left[L - p_{\mathrm{V}} \left(\frac{1}{\rho_{\mathrm{S}}} - \frac{1}{\rho_{\mathrm{L}}}\right)\right]\right\} \frac{\mathrm{d}p_{\mathrm{V}}}{\mathrm{d}t} = Q_{\mathrm{V}} + Q_{\mathrm{IL}}. \tag{A 5}$$

This can be written more compactly as

$$\frac{\mathrm{d}p_{\mathrm{V}}}{\mathrm{d}t} = F(p_{\mathrm{V}})(Q_{\mathrm{V}} + Q_{\mathrm{IL}}), \tag{A 6}$$

where

$$F(p_{\mathrm{V}}) \equiv \left\{\rho_{\mathrm{S}} V c_{\mathrm{V}} \frac{\partial T_{\mathrm{S}}}{\partial p_{\mathrm{V}}} + \frac{\partial}{\partial p_{\mathrm{V}}}(\rho_{\mathrm{S}} V) \left[L - p_{\mathrm{V}} \left(\frac{1}{\rho_{\mathrm{S}}} - \frac{1}{\rho_{\mathrm{L}}}\right)\right]\right\}^{-1} \tag{A 7}$$

only depends on p_{V}.

This can be further simplified by observing that for an ideal gas

$$\frac{\partial T_{\mathrm{S}}}{\partial p_{\mathrm{V}}} = \frac{R_{\mathrm{G}} T_{\mathrm{S}}^2}{L m p_{\mathrm{V}}}, \tag{A 8}$$

$$\frac{\partial}{\partial p_{\mathrm{V}}}(\rho_{\mathrm{S}} V) = \frac{\rho_{\mathrm{L}} V}{\rho_{\mathrm{L}} - \rho_{\mathrm{S}}} \left(\frac{m}{R_{\mathrm{G}} T_{\mathrm{S}}} - \frac{1}{L}\right), \tag{A 9}$$

$$\tag{A 10}$$

by making use of (2.10), (A 1) and (A 2). Substituting these expressions into (A 7) and performing a few more algebraic simplifications results in

$$F(p_{\mathrm{V}}) = \frac{L}{V} \left\{c_{\mathrm{V}} T_{\mathrm{S}} + \left(\frac{L m}{R_{\mathrm{G}} T_{\mathrm{S}}} - 1\right) \frac{\rho_{\mathrm{L}}}{\rho_{\mathrm{L}} - \rho_{\mathrm{S}}} \left[L - p_{\mathrm{V}} \left(\frac{1}{\rho_{\mathrm{S}}} - \frac{1}{\rho_{\mathrm{L}}}\right)\right]\right\}^{-1}. \tag{A 11}$$

REFERENCES

AYDELOTT, J. C. 1967 Effect of gravity on self-pressurization of spherical liquid-hydrogen tankage. *NASA TN* D-4286, 1–18.

AYDELOTT, J. C. 1979 Axial jet mixing of ethanol in cylindrical containers during weightlessness. *NASA TP* 1487.

AYDELOTT, J. C. 1983 Modeling of space vehicle propellant mixing. *NASA TP* 2107.

BURELBACH, J. P., BANKOFF, S. G. & DAVIS, S. H. 1988 Nonlinear stability of evapourating/condensing liquid films. *J. Fluid Mech.* **195**, 463–494.

CHA, Y. S., NEIMAN, R. C. & HULL, J. R. 1993 Thermodynamic analysis of helium boil-off experiments with pressure variations. *Cryogenics* **33**, 675–679.

DELHAYE, J. M. 1974 Jump conditions and entropy sources in two-phase systems. *Intl J. Multiphase Flow* **1**, 395–409.

ENGELMAN, M. S. & SANI, R. L. 1984 Finite element simulation of incompressible flows with free/moving surface. In *Numerical Methods in Laminar and Turbulent Flows*. Pineridge, Swansea.

ENGELMAN, M. S., STRANG, G. & BATHE, K. J. 1981 The application of quasi-Newton methods in fluid mechanics. *Intl J. Numer. Meth. Engng* **17**, 707–718.

GRAYSON, G. D. & NAVICKAS, J. 1993 Interaction between fluid dynamic and thermodynamic phenomena in a cryogenic upper stage. *AIAA Paper* 93-2753.

GRAYSON, G. D., WATTS, D. A. & JURNS, J. M. 1997 Thermo-fluid-dynamic modeling of a contained liquid in variable heating and acceleration environments. *ASME FED* SM97-3567.

GRESHO, P. M., LEE, R. L. & SANI, R. C. 1979 On the time-dependent solution of the incompressible Navier–Stokes equations in two and three dimensions. In *Recent Advances in Numerical Methods in Fluids* (ed. C. Taylor & K. Morgan), vol. 1, pp. 27–79. Pineridge, Swansea.

HOCHSTEIN, J. I., GERHART, P. M. & AYDELOTT, J. C. 1984 Computational modeling of jet induced mixing of cryogenic propellants in low-g. *AIAA Paper* 84-1344.

HUNG, R. J. & LEE, C. C. 1994 Effect of a baffle on slosh waves excited by gravity-gradient acceleration in microgravity. *J. Spacecraft Rockets* **31**, 1107–1114.

HUNG, R. J. & SHYU, K. L. 1992 Constant reverse thrust activated reorientation of liquid hydrogen with geyser initiation. *J. Spacecraft Rockets* **29**, 279–285.

KITTEL, P. & PLACHTA, D. W. 2000 Propellant preservation for mars missions. *Adv. Cryogenic Engng* **45**, 443.

KOTHE, D. B., MJOLSNESS, C. R. & TORREY, M. D. 1991 Ripple: a computer program for incompressible flows with free surfaces. *Los Alamos National Laboratory*, LA-12007-MS.

LIN, C. S. & HASAN, M. M. 1990*a* Numerical investigation of the thermal stratification in cryogenic tanks subjected to wall heat flux. *AIAA Paper* 90-2375.

LIN, C. S. & HASAN, M. M. 1990*b* Vapour condensation on liquid surface due to laminar jet-induced mixing: the effects of system parameters. *AIAA Paper* 90-0354.

LIN, C. S. & HASAN, M. M. 1992 Self pressurization of a spherical liquid hydrogen storage tank in a microgravity environment. *AIAA Paper* 92-0363.

LIN, C. S., HASAN, M. M. & VAN DRESAR, N. T. 1994 Experimental investigation of jet-induced mixing of a large liquid hydrogen storage tank. *AIAA Paper* 94-2079.

LIU, C. H. 1994 A numerical calculation of time dependant dynamical behavior of liquid propellants in a microgravity environment. *Microgravity Sci. Technol.* **7**, 169–172.

MARCHETTA, J. G. & HOCHSTEIN, J. I. 2000 Simulation and dimensionless modeling of magnetically induced reorientation. *AIAA Paper* 2000-0700.

MARCHETTA, J. G., HOCHSTEIN, J. I & SAUTER D. R. 2001 Simulation and prediction of magnetic cryogenic propellant positioning in reduced gravity. *AIAA Paper* 2001-0930.

NAVICKAS, J. 1988 Prediction of a liquid tank thermal stratification by a finite difference computing method. *AIAA Paper* 88-2917.

PETERSON, L. D., CRAWLEY, E. F. & HANSMAN, R. J. 1989 Nonlinear fluid slosh coupled to the dynamics of a spacecraft. *AIAA J. Paper* 88-2470, pp 1230–1240.

PLACHTA, D. 2000 Hybrid thermal control testing of a cryogenic propellant tank. *Adv. Cryogenic Engng* **45**, 465.

POTH, L. J. & VAN HOOK, J. R. 1972 Control of the thermodynamic state of space-stored cryogens by jet mixing. *J. Spacecraft* **9**, 332–336.

Salerno, L. J. & Kittel, P. 1999 Cryogenics and the human exploration of mars. *Cryogenics* **39**, 381–388.

Schrage, R. W. 1953 *A Theoretical Study of Interphase Mass Transfer*. Columbia University Press.

Thornton, R. J. & Hochstein, J. I. 2001 Microgravity propellant tank geyser analysis and prediction. *AIAA Paper* 2001-1132.

Vaughan, D. A. & Schmidt, G. R. 1991 Analytical modeling of no-vent fill process. *J. Spacecraft* **28**, 574–579.